Research paper

Constructing magnetic catalysts with in-situ solid-liquid interfacial photo-Fenton-like reaction over Ag_3PO_4@$NiFe_2O_4$ composites

Shuquan Huang, Yuanguo Xu*, Ting Zhou, Meng Xie, Yun Ma, Qingqing Liu, Liquan Jing, Hui Xu*, Huaming Li

School of Chemistry and Chemical Engineering, Institute for Energy Research, Jiangsu University, Zhenjiang 212013, PR China

A B S T R A C T

A high-performance photocatalyst should be superior not only in light absorption and charge transfer but also surface catalytic reaction. Here we report a green and simple strategy for evenly decorating Ag_3PO_4 particles using magnetic $NiFe_2O_4$ nanoparticles (NPs). The $NiFe_2O_4$ NPs could act as a magnetic support material for recycling the photocatalysts, as well as in situ catalytically decompose the H_2O_2 produced on the surface of Ag_3PO_4 into $O_2 \cdot^-$ and $\cdot OH$ radicals via a photo-Fenton process. The catalytic decomposition of H_2O_2 could produce strong oxidative capacity $O_2 \cdot^-$ and $\cdot OH$ radicals for the organic pollutants degradation and reduce host semiconductor holes ($h^+_{(Ag_3PO_4)}$) consumption by these produced H_2O_2. Thus, the photocatalytic activities of Ag_3PO_4@$NiFe_2O_4$ composites were greatly enhanced. Taking the photocatalytic degradation of Methyl orange (MO), hardly decomposed colorless phenol compounds bisphenol A (BPA) and killing Escherichia coli (*E. coli*) as mode photocatalytic reactions, this system exhibited superior photocatalytic performances than that of pristine Ag_3PO_4. Electron spin resonance (ESR) spectroscopy and sacrificial-reagent incorporated photocatalytic characterizations indicated that the in situ eliminating/active decomposition of H_2O_2 produced by Ag_3PO_4 was the main reason for the enhanced photocatalytic activities.

1. Introduction

Catalytic eliminating of environmental pollutants, such as organic pollutants and pathogenic microorganisms, from water driven by sunlight is considerable popular in recent years [1,2]. The key for this kind of technology is to find out photocatalysts which possess specific features including high activity, good recyclability, high stability and efficient recovery [3,4]. Generally speaking, a semiconductor basically involves three key points related to photocatalysis performance, i.e. light absorption, charge transfer and surface catalytic reaction (or charge consumption) [5,6]. The three sequential and complementary steps are indispensable, and only when all the three are effectively accomplished can the overall performance of a photocatalyst be optimized. Therefore, improving the efficiencies of each step is the fundamental way to develop new, highly efficient photocatalysts. In efforts to extend the light-absorption spectral range, some basic methods have been developed, such as elements doping and the plasmonic effect of noble metals [7–10]. However, the light absorption mainly depends on the nature band gap of a semiconductor, which means a suitable intrinsic band gap is the key of resolving the light absorption problem. For the charge transfer step, built-in electric field can steer the charge kinetics [11–13], 2D nanostructure favors the electrons diffusion [14–18] and the highly crystallized nanocrystal is crucial in accelerating the charge transport [19–22]. In the last step, surface catalytic reaction (or charge consumption), large surface areas are generally beneficial for enhancing reactive sites [23], while the reactive oxygen species (ROSs) generation properties on the surface of photocatalyst are more important for environment purification [24–26]. However, semiconductor materials may nonspecific in catalyzing ROSs production, which suppress the surface catalytic reaction (or charge consumption) efficiency [27]. Therefore, to construct novel photocatalysts that can harvest broad visible light, with good charge transfer property and possess efficient surface catalytic reactive activities for ROSs generation is extremely attractive in the environment purification photocatalysis process.

Silver phosphate (Ag_3PO_4), possesses a suitable band gap of 2.45 eV and can absorb light of wavelength shorter than ca. 530 nm, has been widely studied for oxygen production from water and organic contaminant decomposition [28]. In addition, researchers have found that Ag_3PO_4 possess built-in electric field between PO_4^{3-} ions and Ag^+, which helps e^-/h^+ separation [29]. More importantly, the highly crystallized nanocrystals of Ag_3PO_4 further accelerate the charge

---

transport in the Ag_3PO_4 crystals, which is favorable for its photo-catalytic activity [30]. However, the focuses of recent studies mainly have been on expanding the light absorption range and charge transfer rate on Ag_3PO_4-based photocatalysts [31], the researches of gaining efficient surface catalytic reaction (or charge consumption) for ROSs generation on the surface of Ag_3PO_4 are very rare [32,33]. Nevertheless, the surface catalytic reaction is also an indispensable step for efficient photocatalysis reaction. Therefore, clarification of those questions is very important to further development of a high efficient Ag_3PO_4-based photocatalyst [34]. Pioneer works have demonstrated that the enriching of electrons on Ag_3PO_4 facilitates the multiple-electron reduction reaction of oxygen to form H_2O_2 (Eq. (2)) [35]. However, H_2O_2 is inactive for most organic pollutants (such as MO, BPA and other phenol compounds) degradations (Fig. S1). Even if small amount of the H_2O_2 could self-decomposition to finally form $O_2 \cdot^-$ (Eqs. (3)–(5)) [36], but the $O_2 \cdot^-$ is barely satisfaction generated via this self-decomposition process. More importantly, the low concentration of H_2O_2 would consume the photogenerated $h^+_{(Ag3PO4)}$ (Eq. (7)) which is the dominant active specials in the organic pollutants photocatalysis decomposition process [37]. The pure Ag_3PO_4 thus exhibited a slack photocatalytic activity. Hence, to improve the photocatalytic activities of Ag_3PO_4, the addition of catalysts that can active decomposition of H_2O_2 is crucial.

$$O_2 + H^+ + e^- \rightarrow \cdot OOH \quad (-0.13 \text{ V vs NHE}) \tag{1}$$

$$O_2 + 2H^+ + 2e^- \rightarrow H_2O_2 \quad (0.68 \text{ V vs NHE}) \tag{2}$$

$$H_2O_2 \rightarrow H^+ + HO_2^- \tag{3}$$

$$HO_2^- \rightarrow e^- + HO_2 \cdot \tag{4}$$

$$HO_2 \cdot \rightarrow H^+ + O_2 \cdot^- \tag{5}$$

$$2H_2O_2 \rightarrow H_2O + O_2 \tag{6}$$

$$H_2O_2 + 2h^+_{(Ag3PO4)} \rightarrow O_2 + 2H^+ \tag{7}$$
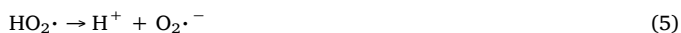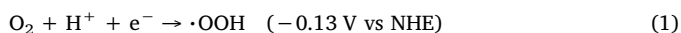
Herein, we report the successful decoration of magnetic p-type semiconductor nickel ferrite $NiFe_2O_4$ nanoparticles (NPs) on the surface of Ag_3PO_4. The $NiFe_2O_4$ NPs possess specific in catalytic decomposing H_2O_2 properties under visible light irradiation, which can effectively catalyze the decomposition of H_2O_2 into $O_2 \cdot^-$ and $\cdot OH$ radicals via a photo-Fenton process (Eqs. (8)–(12)) [38–40], just as the report of surface-decorated Fe^{3+} as a trigger of H_2O_2 conversion over the alkalinized-CN&Fe system by Li et al. [41] Accordingly, the consumption of $h^+_{(Ag3PO4)}$ by the adsorbed H_2O_2 processes on the surface of Ag_3PO_4 has been inhibited, instead of this, a great mount of $O_2 \cdot^-$ and $\cdot OH$ radicals could be generated for the organic degradation. This approach therefore improved the surface reactions of Ag_3PO_4 and enhanced its photocatalytic activities. In addition, once O_2 is consumed for H_2O_2 production, it would be immediately supplied from air. Accordingly, the reaction process can be described via first-order kinetic reaction. The versatile magnetic properties of $NiFe_2O_4$ could help recycling the $Ag_3PO_4@NiFe_2O_4$ composites via a magnetic field. Methyl orange (MO), hardly decomposed colorless phenol compounds bisphenol A (BPA) and the Escherichia coli (E. coli) were chosen as the mode pollutant substrates to evaluate the photocatalytic performance. The results showed that the $Ag_3PO_4@NiFe_2O_4$ composites exhibited much higher photocatalytic performance than that of pure Ag_3PO_4. In this work, we try to highlight that the $NiFe_2O_4$ NPs in the $NiFe_2O_4@Ag_3PO_4$ composites not only serve as a band-edges matched semiconductor for enhancing the separation rate of electron−hole pairs, but also act as a specific component in catalyzing decomposing of H_2O_2. The insight photocatalytic mechanisms were discussed in detail by using colorimetric N, N-diethyl-p-phenylenediamine (DPD) method, ESR analysis and comprehensive trapping experiments. These findings may open a new sight for the studies of the complex photocatalytic reaction mechanisms and kinetics.

$$NiFe_2O_4 + h\nu \rightarrow e^- + h^+ \tag{8}$$

$$Fe^{3+} + e^-_{(NiFe_2O_4)} \rightarrow Fe^{2+} \tag{9}$$

$$Fe(OH)^{2+} + h\nu \rightarrow Fe^{2+} + \cdot OH \tag{10}$$

$$Fe^{2+} + H_2O_2 \rightarrow Fe^{3+} + \cdot OH + OH^- \quad (K \approx 70 \text{ M}^{-1}\text{ s}^{-1}) \tag{11}$$

$$Fe^{3+} + H_2O_2 \rightarrow Fe^{2+} + \cdot OOH + H^+ \quad (K = 0.001\text{–}0.01 \text{ M}^{-1}\text{ s}^{-1}) \tag{12}$$
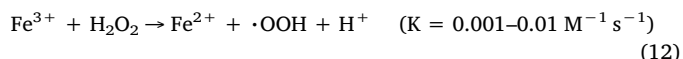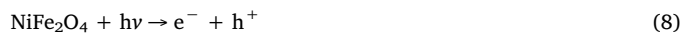
2. Experimental section

2.1. Synthesis of $NiFe_2O_4$ NPs

In a typical of process, 2.10 g $FeCl_3 \cdot 6H_2O$, 0.90 g $NiCl_2 \cdot 6H_2O$ and 5.40 g cyclodextrin were dissolved in 90 mL distilled water via vigorous magnetic stirring. Then the pH of the solution was adjusted to 13 using 6 M NaOH solution. Then the suspensions were further stirred for another 2 h. Subsequently, the suspensions were transferred into two 50 mL stainless steel autoclave and kept at 160 °C for 24 h. After the temperature was cool down, the precipitates were washed with deionized water until the pH = 7 and dried at 60 °C. The resulting powder was then put into an alumina crucible and calcined for 2 h at a temperature of 550 °C.

2.2. Synthesis of $Ag_3PO_4@NiFe_2O_4$ composite material

The $Ag_3PO_4@NiFe_2O_4$ composites were prepared via a simple and green hydrothermal method. Typically, 0.4 g $AgNO_3$ was dissolved in 30 mL deionized water. Then, a certain amount of the as-prepared $NiFe_2O_4$ NPs was distributed in above solution by ultrasonic treatment. After that, the suspension was stirred for 30 min. Subsequently, 3 mL Na_3PO_4 solution (1 g/mL) were added into the mixture drop by drop and kept stirring for 1 h. It should be noted that the whole experiments were kept at 60 °C with a circulating water system. After the precipitation process, these obtained precipitates were transferred to 25 mL Teflon-lined stainless steel autoclaves and kept for 2 h at 120 °C. After cooling to room temperature, the precipitate was washed with distilled water and ethanol for several times, and then dried at 60 °C in a vacuum oven overnight. The final products were named as 1% $Ag_3PO_4@NiFe_2O_4$, 3% $Ag_3PO_4@NiFe_2O_4$ and 5% $Ag_3PO_4@NiFe_2O_4$ according to the mass fraction of $NiFe_2O_4$ in the weight of $AgNO_3$.

2.3. Photocatalytic activity measurement and kinetics

The photocatalytic activities of the as-prepared photocatalysts were examined toward photodegradation of MO and BPA in aqueous solution under visible light irradiation ($\lambda > 420$ nm, 300 W xenon lamp). Typically, 0.02 g as-prepared photocatalysts were added into an MO (80 mL, 10 mg L^{-1}) or BPA (80 mL, 10 mg L^{-1}) aqueous solution, and sonicated for 5 min to disperse the photocatalysts completely, followed by stirring under dark condition for 30 min to achieve the saturated adsorption. After that, turned on the lamp and 4 mL aliquots were extracted from each sample at regular intervals and centrifuged to remove the catalysts. During the photoreactions, the experiment temperature were kept at 30 °C by using a circulating water system. And an air pump was employed to offer oxygen. The concentrations of MO were analyzed on a UV–vis spectrophotometer (UV-2450, Shimadzu) at wavelength 463 nm. An Agilent TC-C18 column with two Varian ProStar 210 pumps and a Varian ProStar 325 UV–vis Detector was used to analyze the concentration of BPA at wavelength 230 nm. The mobile phase was 1 mL min^{-1} with a solution of methanol and H_2O (v: v = 75: 25). The MO or BPA degradation rates (E) over the photocatalysts were calculated via the equation below:

$$E = (1 - C/C_0) \times 100\% = (1 - A/A_0) \times 100\% \qquad (13)$$

where C and C_0 are the solution concentration at time t and t_0 during the reaction, A and A_0 are the corresponding values of absorbency.

The MO or BPA degradation rate constant (k) over the photocatalysts were calculated via the equation below:

$$k = \frac{1}{t} \ln \frac{C}{C_0} \qquad (14)$$

where C and C_0 are the solution concentrations when reaction time is t and 0, respectively.

2.4. Photocatalytic disinfection performance

Before experiment, all glass apparatuses and culture medium solution used in the experiments were sterile. The bacterial cells were grown in nutrient broth at 37 °C for 16 h under agitating at 200 rpm to yield a cell count of approximately 10^9 colony forming units (cfu)/mL. Subsequently, the sample was leaded to $1*10^7$ via serially diluting with sterilized saline solution.

The photocatalytic disinfection activities of $Ag_3PO_4@NiFe_2O_4$ composites were conducted by photoinduce killing *E. coli* bacteria under visible light ($\lambda > 420$ nm, 300 W xenon lamp). Typically, 0.5 mg as-prepared samples were dispersed in 20 mL diluted bacterial solution. Before irradiation, the suspensions were magnetically stirred for 30 min in the dark. During the photoreactions, 20 μL suspensions were evenly spread on nutrient agar plates at the time of 0 min, 5 min, 10 min, and 20 min, respectively, and then these plates were then incubated at 37 °C for 16 h in dark.

3. Results and discussion

3.1. Crystal structures information

The XRD technology was employed to characterize the purity and crystallinity of the as-prepared samples. Fig. 1 shows the XRD patterns of pure Ag_3PO_4, $Ag_3PO_4@NiFe_2O_4$ composites and $NiFe_2O_4$. For the XRD pattern of pure Ag_3PO_4 (Fig. 1d), the obvious peaks at $2\theta = 20.8°$, 29.7°, 33.3°, 36.5°, 42.5°, 47.8°, 52.7°, 55.0°, 57.3°, 61.6°, 65.8°, 69.9°, 71.9°, 73.8° and 77.7° represent (110), (200), (210), (211), (220), (310), (222), (320), (321), (400), (411), (420), (421), (332) and (422) crystal planes of the body-centered cubic phase of Ag_3PO_4 (JCPDS No. 84-0510) (marked with red ★), respectively [42]. The patterns of $Ag_3PO_4@NiFe_2O_4$ composites (Fig. 1a–c) are much nearly identical to those of pure Ag_3PO_4, suggesting the loading of $NiFe_2O_4$ NPs did not

Fig. 1. XRD profiles of the as-prepared samples: a. pure Ag_3PO_4, b. 1% $Ag_3PO_4@NiFe_2O_4$ composite, c. 3% $Ag_3PO_4@NiFe_2O_4$ composite, d. 5% $Ag_3PO_4@NiFe_2O_4$ composite, e. $NiFe_2O_4$. (For interpretation of the references to colour in the text, the reader is referred to the web version of this article.)

turned the phase of Ag_3PO_4 or incorporated into the lattice of Ag_3PO_4. For the XRD pattern of pure $NiFe_2O_4$ (Fig. 1e), all the diffraction peaks can be indexed into the plans of spinel-type $NiFe_2O_4$ (JCPDS No. 54-0964) (marked with black ◆). In addition, the peaks of $NiFe_2O_4$ are ambiguously observed in the $Ag_3PO_4@NiFe_2O_4$ composite materials, which should be ascribed to the high crystallinity diffraction peaks of Ag_3PO_4 and the low content of $NiFe_2O_4$ in the hybrid system. [43]

3.2. Morphology and textural property

SEM was employed to investigate the morphology and surface textural of the as-prepared samples. The morphology of $NiFe_2O_4$ NPs was showed in Fig. S2, which is granular like nanoparticles with diameters of ca. 20–50 nm. Typical SEM images of pure Ag_3PO_4 and 3% $Ag_3PO_4@NiFe_2O_4$ composite are displayed in Fig. 2. From the low magnification SEM image of pure Ag_3PO_4 (Fig. 2A), it can be seen that the as-prepared pure Ag_3PO_4 are regular sphere particles with a diameter of about 2 μm. By close observation (Fig. 2B), these particles are polyhedral morphology with smooth surface. For the SEM images of 3% $Ag_3PO_4@NiFe_2O_4$ composite, there is no big difference can be observed in the low magnification SEM images (Fig. 2C) with that of pure Ag_3PO_4, indicating the introduction of $NiFe_2O_4$ NPs did not affected the main morphology of Ag_3PO_4 obviously in the synthesis process. While in the high magnification SEM image (Fig. 2D), it can be clearly seen that the $NiFe_2O_4$ NPs were evenly distributed throughout the whole surface of Ag_3PO_4 particles and tightly attached, illustrating their compound structure [44]. At the meantime, EDS mapping was carried out to further verify the evenly distribution of $NiFe_2O_4$ NPs, as shown in Fig. 3, it is clearly that Ag, P, O, Fe and Ni elements distribute homogeneously within the particle of $Ag_3PO_4@NiFe_2O_4$ composite, which offers direct visual evidence for the evenly distribution of Ni and Fe elements within the composite. Moreover, it is a compelling evidence that the uniformly distribution and tightly attaching of $NiFe_2O_4$ on the surface of Ag_3PO_4 particles is beneficial to the as-prepared $Ag_3PO_4@NiFe_2O_4$ composite can be totally separated from solution by an extra magnetic field.

3.3. Chemical coordination analysis

In order to further verify the surface elements compositions and chemical states of the as-prepared samples, X-ray photoelectron spectroscopy (XPS) technology was employed. The binding energies of the XPS spectra have corrected for specimen charging by referencing the C 1s line to 284.6 eV. From the XPS survey spectra (Fig. 4A), it is clearly that the $Ag_3PO_4@NiFe_2O_4$ composite is composed of Ag, P, O, Fe, Ni and C elements, of which the C element is assigned to residual carbon from the XPS instrument. Fig. 4B shows that the Ag 3d spectra consisted of two individual peaks at approximately 368.2 and 374.1 eV, which could be ascribed to binding energies of Ag 3d5/2 and Ag 3d3/2, respectively. It is worthwhile to note that in the cases of Ag 3d spectra, about 0.2 eV negative shifts have been observed in the spectra of 3% $Ag_3PO_4@NiFe_2O_4$ composite compare to that of pure Ag_3PO_4, suggesting the chemical environments of Ag^+ have changed. The negative shifts in the binding energy of Ag 3d in the 3% $Ag_3PO_4@NiFe_2O_4$ composite might be attributed to the interaction of Ag^+ ions with the rich-electronic structure $NiFe_2O_4$ nanoparticles, similar results have been observed in previous works [43,45,46]. Furthermore, the intensities of Ag 3d in the 3% $Ag_3PO_4@NiFe_2O_4$ composite are much lower than that of Ag_3PO_4. Similar phenomenon also can be observed on the P 2p spectra (Fig. S3). Considering that the XPS signals were mainly collected from the surface of the sample with depth less than 10 nm, the decreased Ag 3d and P 2p spectra signals again verified the $NiFe_2O_4$ NPs were attached on the surface of Ag_3PO_4 [47]. High-resolution XPS spectra of Fe and Ni for the $Ag_3PO_4@NiFe_2O_4$ composite are shown in Fig. 4C and D, respectively. Both Fe 2p and Ni 2p exhibit complex shake-up satellite structures arising from multiplet interactions between the core hole generated on photoemission and the unpaired 3d
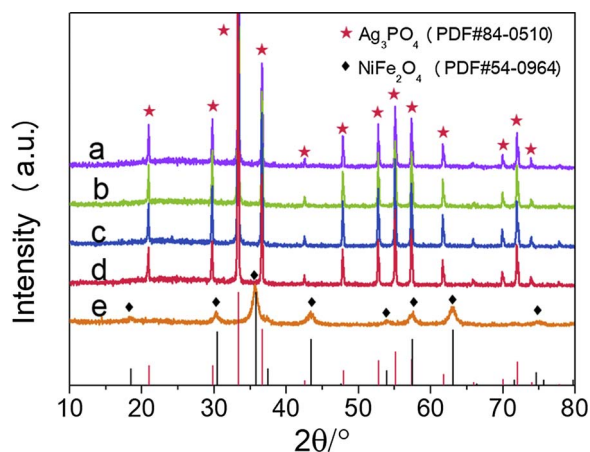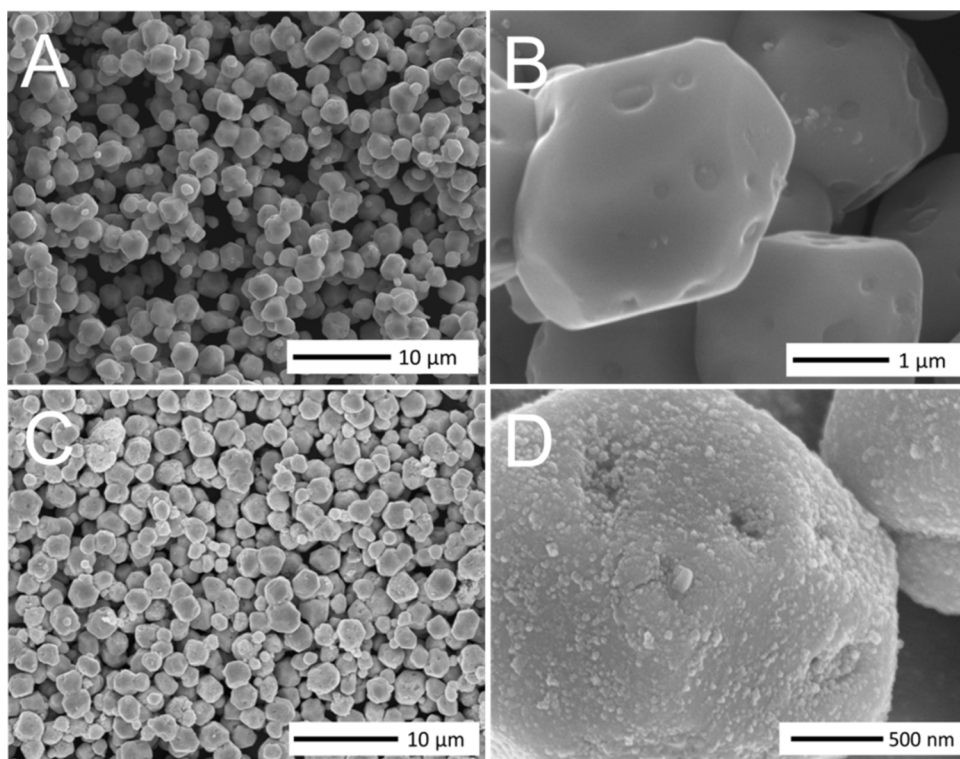
valence electrons. Indicating the high spin Fe^{3+} and Ni^{2+} centres contain in the samples [39,48].

3.4. Optical properties

Fig. 5A displays the DRS spectra of the pure Ag_3PO_4, pure $NiFe_2O_4$ and $Ag_3PO_4@NiFe_2O_4$ composites. The typical UV–vis spectra of pure Ag_3PO_4 shows an absorption region ranging from 200 nm to 530 nm, which is originates from the intrinsic charge transfer response of Ag_3PO_4 from the valence band to the conduction band [28]. The pure $NiFe_2O_4$ possesses strong and wider absorption in the visible region, which can be attributed to the narrow band gap of $NiFe_2O_4$ [49]. Compare to pure Ag_3PO_4, the optical absorption of $Ag_3PO_4@NiFe_2O_4$ composites was gradually enhanced with the boosting of $NiFe_2O_4$

loading content. The expansion of light absorption is normally in turn promotes the utilization efficiency of solar light and good for the photocatalytic activities [50,51]. Fig. 5B is the corresponding Tauc's plots of $(ahv)^2$ vs. (hv) of $NiFe_2O_4$ and Ag_3PO_4, which displayed that the band gap of $NiFe_2O_4$ and Ag_3PO_4 were determined to be 1.70 eV and 2.45 eV, respectively.

3.5. Photocatalytic performance tests

To assess the validity of the $NiFe_2O_4$ modification on enhancing the photocatalytic performance, photocatalytic degradation of MO was carried out over the as-synthesized photocatalysts. The results are shown in Fig. 6A. Obviously, these $Ag_3PO_4@NiFe_2O_4$ composites showed improved photocatalytic performance than that of pure
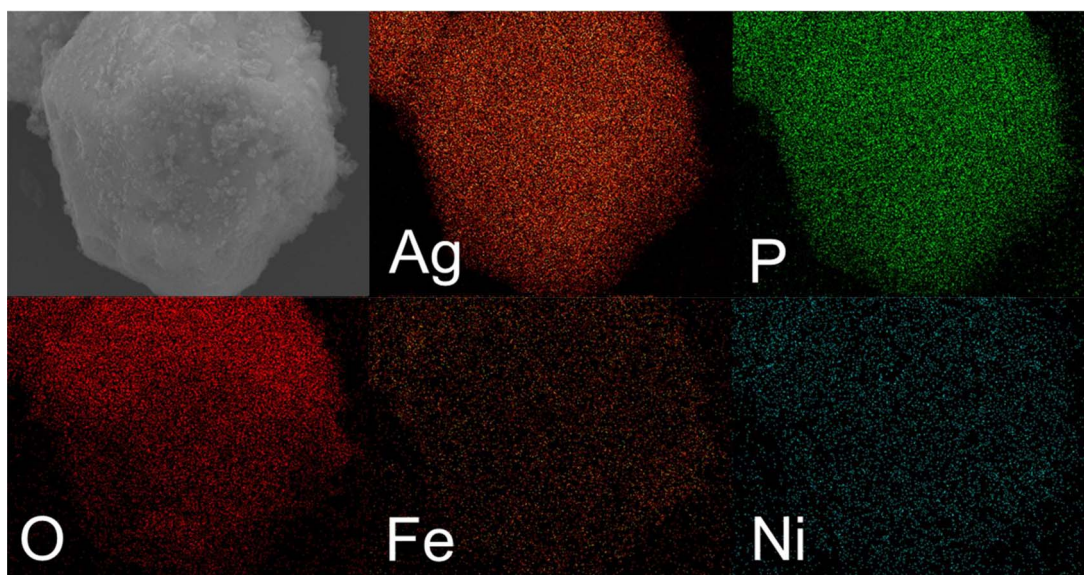

Fig. 3. EDS mappings of the 3% $Ag_3PO_4@NiFe_2O_4$ composite.

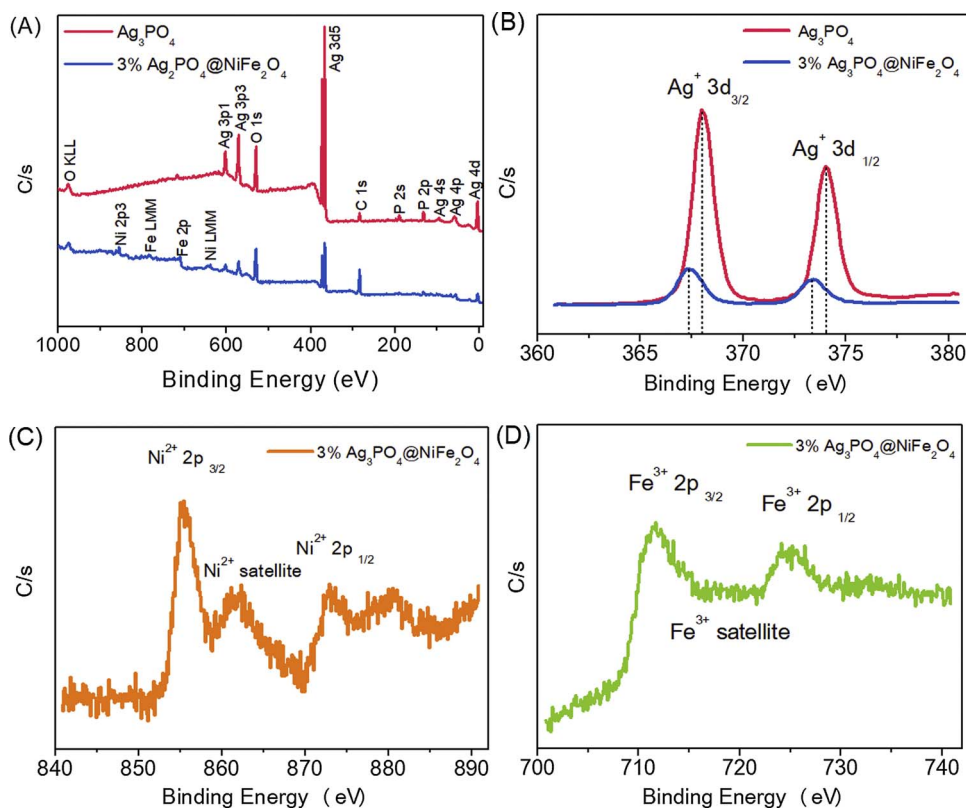**Fig. 4.** XPS spectra of the as-prepared samples: (A) survey, (B) Ag 3d, (C) Ni 2p, (D) Fe 2p.

Ag_3PO_4. After light illumination for 30 min ($\lambda > 420$ nm), the MO degradation rate were 64.2%, 85.2%, 96.8% and 93.8% over the pure Ag_3PO_4, 1% $Ag_3PO_4@NiFe_2O_4$, 3% $Ag_3PO_4@NiFe_2O_4$, and 5% $Ag_3PO_4@NiFe_2O_4$ composite, respectively. The 3% $Ag_3PO_4@NiFe_2O_4$ composite possesses the optimum photocatalytic performance. The photodegradation of MO as well as BPA follow a pseudo-first-order kinetics behavior (detailed mechanism study will be introduced in the mechanism discussion section). The values of the pseudo-first-order rate constant (k) for the photodegradation of MO over different $NiFe_2O_4$ content are shown in Fig. 6B (Fig. S4A). It can be seen that the 3% $Ag_3PO_4@NiFe_2O_4$ composite showed the highest degradation rate ($k = 0.12$ min^{-1}), about 3 times degradation rate higher than that of pure Ag_3PO_4 ($k = 0.04$ min^{-1}). The excessed $NiFe_2O_4$ will cause the photocatalyst activity to decrease. This phenomenon can be explained that the loading of $NiFe_2O_4$ will promote the utilization of photoelectrons but also suppress the light absorption of semiconductor host, and thus, it should appear an optimal balance between these two contradictory factors at a certain loading amount of $NiFe_2O_4$ (3%). In order to eliminate the photosensitization, colorless organic molecule, BPA, was chosen as a model substance to evaluate the photocatalytic activities. As

shown in Fig. 6C, the photocatalytic performance of the as-prepared samples also exhibited a hump-like photocatalytic activity depending on the loading amount of $NiFe_2O_4$ with 3% as the optimum amount ($k = 0.12$ min^{-1}), which showed 6 times as high as that of pure Ag_3PO_4 ($k = 0.02$ min^{-1}) (Fig. 6D and Fig. S4B).

For the most active 3% $Ag_3PO_4@NiFe_2O_4$ sample, we also evaluated the photocatalytic water disinfection performance. Because of the human health drinking water must be free of pollutants pathogenic bacteria and organics, the remove of different organic pollutants and bacteria simultaneously is useful. Fig. 7 shows the direct results of photocatalytic antibacterial effects of visible light, pure Ag_3PO_4 and 3% $Ag_3PO_4@NiFe_2O_4$ composite toward *E. coli*. It is clear that the number of *E. coli* was not decreased under the visible light irradiation (Fig. 7a), which means the *E. coli* can survive under visible-light irradiation. After contacting with Ag_3PO_4 (Fig. 7b) for 30 min in dark ($Ag_3PO_4 - 0$ min), most *E. coli* colony forming units still can be observed, indicating that the *E. coli* can survive with the low concentration of Ag_3PO_4 in the dark. When the light was turned on, the number of surviving bacteria colony forming units was decreased gradually, but the *E. coli* colony cannot be totally inactivated. On the contrary, when the presented photocatalyst
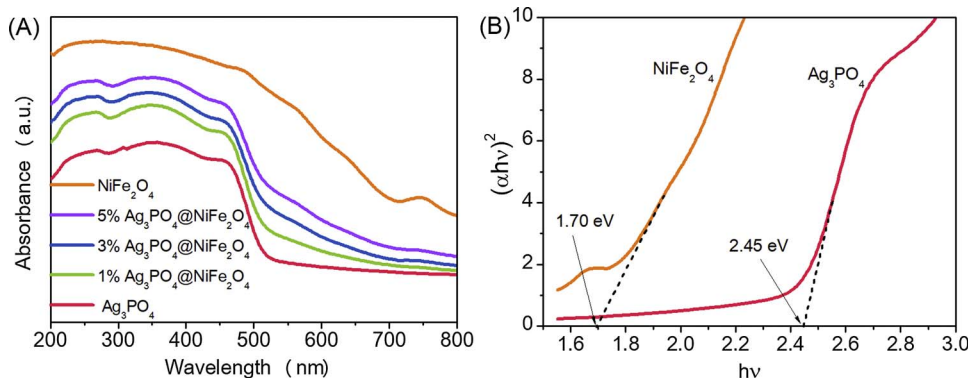

Fig. 5. (A) UV–vis diffuses reflectance spectra of the as-prepared samples. (B) Plots of $(\alpha h\nu)^2$ versus energy ($h\nu$) of the as-prepared $NiFe_2O_4$ and Ag_3PO_4.
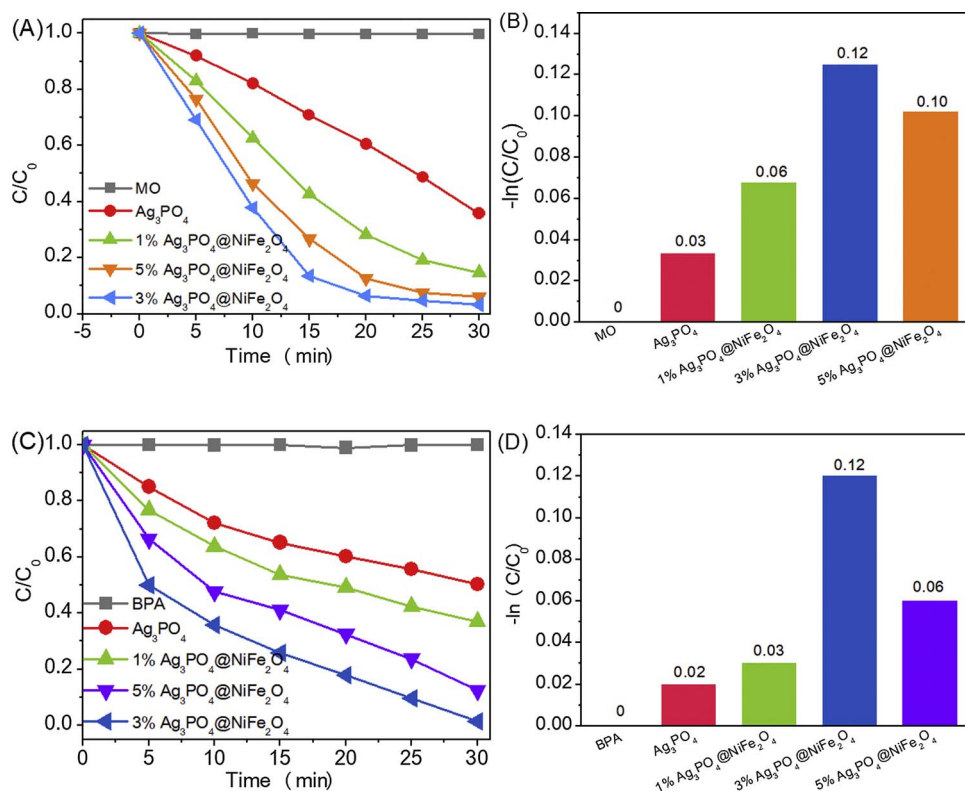
Fig. 6. (A) Photocatalytic degradation of MO by the as-prepared samples. (B) Comparison of the corresponding MO degradation kinetics. (C) Photocatalytic degradation of BPA by the as-prepared samples. (D) Comparison of the corresponding BPA degradation kinetics.

is 3% $Ag_3PO_4@NiFe_2O_4$ composite the inactivated effects were enhanced. As shown in Fig. 7c, after contacted with 3% $Ag_3PO_4@NiFe_2O_4$ composite in the dark for 30 min, lots of bacteria colonies forming units were still observed. Suggesting low concentration of the 3% $Ag_3PO_4@$ $NiFe_2O_4$ composite will not be enough for complete bacterial inactivation in a short period of time. While the surviving bacteria colony forming units were sharply decreased under the visible light irradiation in the presence of 3% $Ag_3PO_4@NiFe_2O_4$ composite, and the *E. coli*

colony have been totally inactivated after 20 min. These results of antibacterial experiments indicate the 3% $Ag_3PO_4@NiFe_2O_4$ composite possesses enhanced antibacterial effects against *E. coli* compare to that of pure Ag_3PO_4.

3.6. A Z-scheme process for enhancing the stability

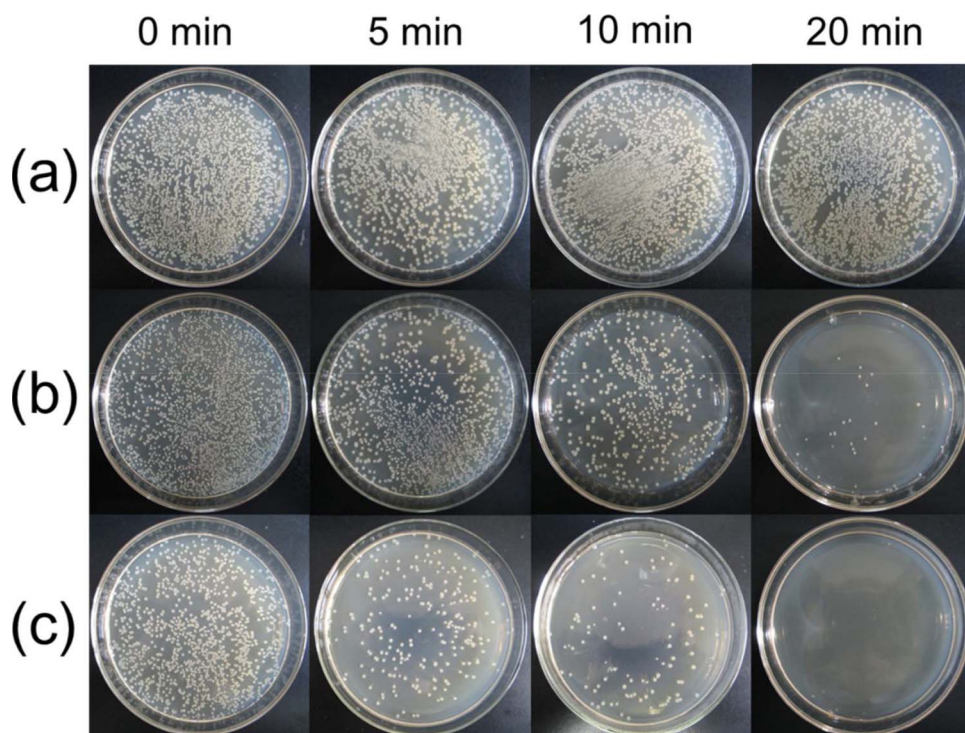Fig. 8A and B are the magnetic separation demonstration images of

Fig. 7. The photocatalytic antibacterial activities of (a) light only, (b) pure Ag_3PO_4 and (c) 3% $Ag_3PO_4@$ $NiFe_2O_4$ composite against *E. coli* at different irradiation times.
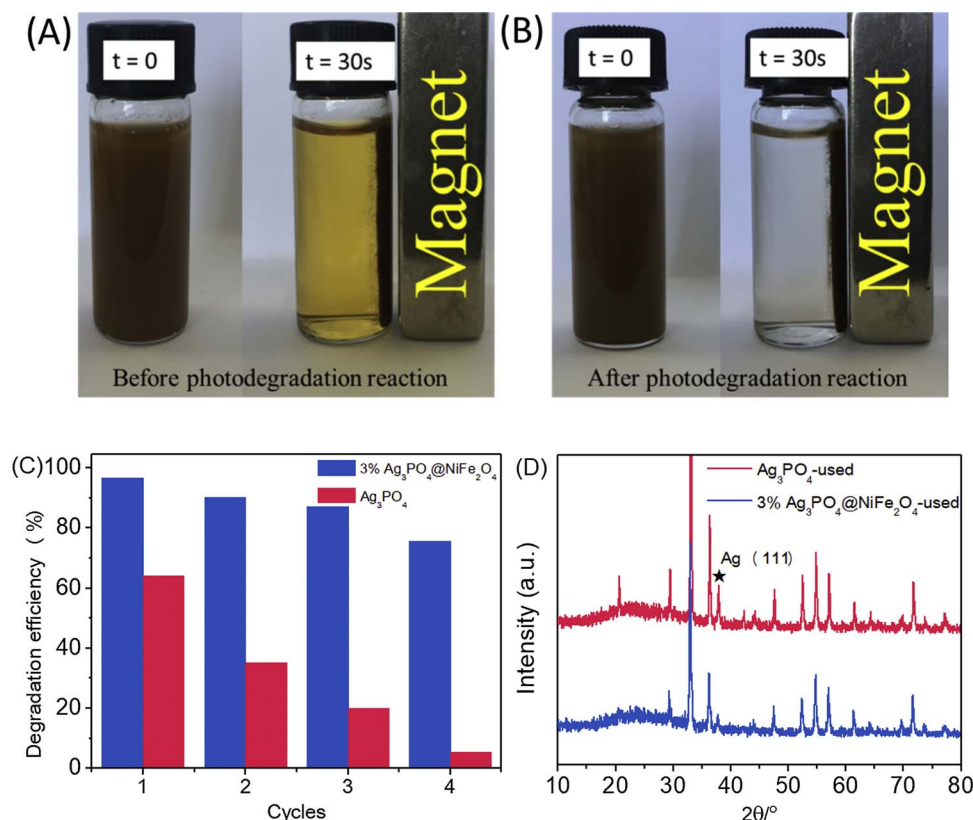
the 3% Ag_3PO_4@$NiFe_2O_4$ composite before and after the MO photodegradation reactions, respectively. It is clear that either fresh or used as-prepared 3% Ag_3PO_4@$NiFe_2O_4$ composite could be separated from the solutions easily by employing magnetic field within 30 s, indicating the Ag_3PO_4@$NiFe_2O_4$ composites possess good structure stabilities and recyclability. For the photocatalytic degradation of BPA, it has the same magnetic recovery function. Fig. 8C displays cycle runs of MO degradation on pure Ag_3PO_4 and 3% Ag_3PO_4@$NiFe_2O_4$. The MO degradation capacity of Ag_3PO_4 significantly decreased after 4 cycles. However, the MO degradation efficiency after the 4 runs was still over 75% on 3% Ag_3PO_4@$NiFe_2O_4$ composite, indicating that the stability of Ag_3PO_4 has been improved. Just like the systems of Ag_3PO_4/CeO_2 [52], Ag_3PO_4/Co_3O_4 [53] and Ag_3PO_4/g-C_3N_4 [54]. According to reports, the stabilities of Ag_3PO_4 are mainly decided by two factors: the photocorrosion effect and the dissolution effects. Firstly, the photocorrosion effect. The main reason for the photocorrosion effect of Ag_3PO_4 is the photogenerated electrons on the CB of Ag_3PO_4 can reduce Ag^+ ions in Ag_3PO_4 to Ag metal. Therefore, we compared the XRD patterns of the used Ag_3PO_4 and 3% Ag_3PO_4@$NiFe_2O_4$ composite samples. As shown in Fig. 8D, the peak that belongs to the metallic Ag ($2\theta = 38.1°$) appeared in both patterns, but the intensity of the used 3% Ag_3PO_4@$NiFe_2O_4$ composite sample is weaker than that of used Ag_3PO_4. Therefore, we speculate that the photocorrosion effect has been inhibited to some degree in the 3% Ag_3PO_4@$NiFe_2O_4$ composite. Secondly, the dissolution effects. Since the Ag_3PO_4 possesses high Ksp of 1.6×10^{-16} under room temperature [55], we further tested the concentrations of Ag^+ in the photocatalytic process of MO degradation over Ag_3PO_4 and 3% Ag_3PO_4@$NiFe_2O_4$ composite were conducted by using AAS. The results are shown in Fig. S5, the Ag^+ concentration of 3% Ag_3PO_4@$NiFe_2O_4$ composite is a litter higher than that of Ag_3PO_4 under visible light irradiation, indicating the introduction of $NiFe_2O_4$ will not prevent the dissolutions of Ag_3PO_4. But, from the results of cycle experiments, the stability has been improved precisely. Therefore, we suggested that the inhibited photocorrosion effect of Ag_3PO_4 by adding $NiFe_2O_4$ is the dominant reason of the improved stability. The

next question is how to inhibit the photocorrosion effect of Ag_3PO_4 in the Ag_3PO_4@$NiFe_2O_4$ composites by introducing $NiFe_2O_4$.

In this system, we proposed a Z-scheme process to explain the photocorrosion inhibit effect. First, as shown in Fig. S6, the CB and VB position of $NiFe_2O_4$ are at -0.60 V vs NHE and 1.10 V vs. NHE, respectively [56]. The CB and VB position of Ag_3PO_4 are at 0.45 V vs NHE and 2.90 V vs. NHE, respectively [28]. Commonly, according to the band structure of Ag_3PO_4 and $NiFe_2O_4$, two different models of semiconductor–semiconductor junctions can be utilized to descript the charge transfer process: Type II and Z-scheme. If it is the Type II model, the photogenerated electrons from the CB of $NiFe_2O_4$ will migrate to the CB of Ag_3PO_4. However, according to the report [31], coupling Ag_3PO_4 with other semiconductors to construct a heterojunction structure can increase the stability of Ag_3PO_4 if the photogenerated electrons have been transferred instead of reducing Ag^+ ions in Ag_3PO_4 to Ag metal. Therefore, it can be reasonable speculate that the electrons should not be transferred from $NiFe_2O_4$ to Ag_3PO_4, in fact, the photogenerated electrons should be transferred from Ag_3PO_4 to $NiFe_2O_4$ (Fig. S7). Thus, the stability was improved. Of course, this process is belonging to the Z-scheme [5]. In addition, the photocurrent responses also provide this Z-scheme junction, which the response of the 3% Ag_3PO_4@$NiFe_2O_4$ composite is much higher than both signal Ag_3PO_4 and $NiFe_2O_4$ under visible light irradiation in the next section [57].

3.7. Structure–activity relationships

To gain insight into the enhancement of photocatalytic activity, the transfer and utilization of the photocarriers were explored. From Fig. 9A, it is clearly that the photocurrent response of the 3% Ag_3PO_4@$NiFe_2O_4$ composite is much higher than that of the pure Ag_3PO_4 and $NiFe_2O_4$ under visible light irradiation (the photocurrent signal of $NiFe_2O_4$ is so weak that it has been covered in Fig. 9A, it has been showed in the inset Figure top right corner). The distinguished photocurrent density implies that more efficient charge separation and migration have gained by the 3% Ag_3PO_4@$NiFe_2O_4$ composite, suggesting
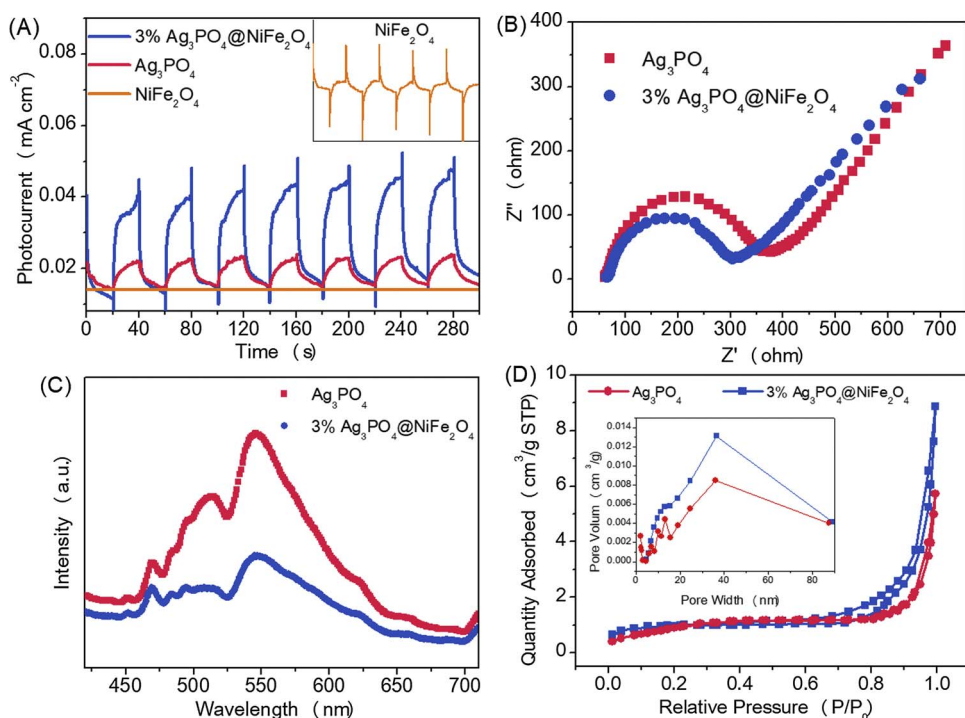
Fig. 9. (A) Photocurrents of $NiFe_2O_4$, Ag_3PO_4 and 3% $Ag_3PO_4@NiFe_2O_4$ composite. (B) Electrochemical impedance spectroscopy of Ag_3PO_4 and 3% $Ag_3PO_4@NiFe_2O_4$ composite. (C) PL spectra of Ag_3PO_4 and 3% $Ag_3PO_4@NiFe_2O_4$ composite. (D) Nitrogen absorption−desorption isotherm of as-prepared Ag_3PO_4 and 3% $Ag_3PO_4@NiFe_2O_4$ composite.

the surface decorating of $NiFe_2O_4$ NPs is favorable for the photoexcited electron-hole pairs separation. In addition, it is noteworthy that the response behaviors of the 3% $Ag_3PO_4@NiFe_2O_4$ composite exhibited an amplification as well as a unification of Ag_3PO_4 and $NiFe_2O_4$ response behaviors, which means both the photocurrent responses of the Ag_3PO_4 and $NiFe_2O_4$ component have been greatly enhanced in the 3% $Ag_3PO_4@NiFe_2O_4$ composite. This result confirmed the synergistic effect between the Ag_3PO_4 and $NiFe_2O_4$ have been formed again. The interfacial charge transfer properties were revealed by electrochemical impedance spectroscopy measurements, as shown in Fig. 9B, the arc radius of the 3% $Ag_3PO_4@NiFe_2O_4$ composite was smaller than that of Ag_3PO_4, indicating the 3% $Ag_3PO_4@NiFe_2O_4$ composite had a better interfacial charge transfer properties [54,58].
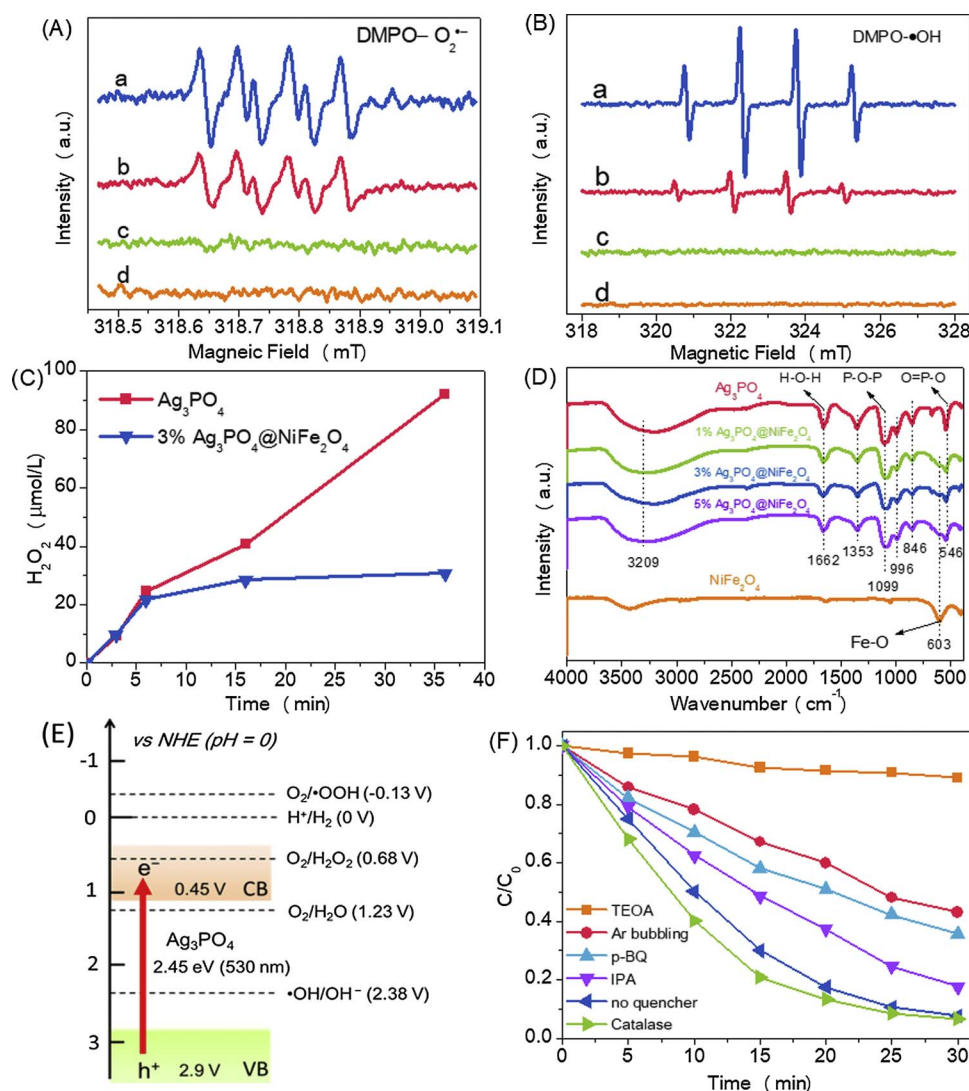
Moreover, we further detected the photoluminescence spectra of pure Ag_3PO_4 and 3% $Ag_3PO_4@NiFe_2O_4$ composite. As displayed in Fig. 9C, a steady and strong PL emission plots around 545 nm can be seen on the pure Ag_3PO_4 spectrum, indicating pure Ag_3PO_4 possess a high charge recombination rate on the surface. On the contrary, the PL emission intensity of 3% $Ag_3PO_4@NiFe_2O_4$ composite is dramatically weakened compared with that of Ag_3PO_4, which means the charge recombination on the surface of 3% $Ag_3PO_4@NiFe_2O_4$ composite have been suppressed. The results of photocurrent−time response, EIS as well as PL indicate that the surface-decorating of $NiFe_2O_4$ NPs can remarkably enhance the separation efficiency of photogenerated electron–hole pairs in Ag_3PO_4.

Considering that specific surface area of the semiconductor was also an important factor which can affect the photocatalytic activity. The specific surface area and porosity of the as-prepared materials were investigated by nitrogen adsorption and desorption. As shown in Fig. 9D, Type IV isotherms can be observed, the corresponding Brunauer–Emmett–Teller (BET) specific surface of 3% $Ag_3PO_4@NiFe_2O_4$ composite was calculated to be 3.6217 m^2/g, which is similar to that of Ag_3PO_4 (3.5042 m^2/g). The pore size distribution curves were shown in the inset figure, it can be found that the introduction of $NiFe_2O_4$ NPs did not obviously affect the pore size and pore volume. Therefore, in this system, the BET surface area may be not the main factors to determining the photocatalytic activity.

3.8. In situ solid-liquid interfacial photo-Fenton-like reaction

Although the charge transfer property was a main factor of improving photocatalytic performance, the contribution of surface reaction kinetics was indispensable. Therefore, we further explored the ROSs production properties over the as-prepared photocatalysts. Fig. 10(A and B) display the ESR spin-trap signals of $O_2\cdot^-$ and $\cdot OH$ over the Ag_3PO_4 and 3% $Ag_3PO_4@NiFe_2O_4$ composite, respectively. It is clear that there are no signal could be observed in the dark condition and the six characteristic peaks of the $DMPO-O_2\cdot^-$ as well as the four characteristic peaks of the $DMPO-\cdot OH$ could be observed on both pure Ag_3PO_4 and 3% $Ag_3PO_4@NiFe_2O_4$ composite samples under visible light irradiation, which mean the $O_2\cdot^-$ and $\cdot OH$ species can be generated on the surface of these two samples under visible light irradiation. Interestingly, the signal intensities of $DMPO-O_2\cdot^-$ and $DMPO-\cdot OH$ were enhanced after the addition of $NiFe_2O_4$, which can be reasonable explained as follows: the conduct band (CB) position of Ag_3PO_4 was + 0.45 V vs. NHE [28], and the potential of the one-electron reduction of O_2 is − 0.13 V vs. NHE (Eq. (1)) [59]. Theoretically, the one-electron reduction of O_2 on the CB edge of Ag_3PO_4 was not allowed in thermodynamics (Fig. 10E). Therefore, the two-electron reduction of O_2 to produce H_2O_2 (0.68 V vs. NHE) on the surface of Ag_3PO_4 would be the main reduction reaction process [35]. Subsequently, in the absence of $NiFe_2O_4$, the photogenerated H_2O_2 could self-decomposition to form a proton and HO_2^- that continues to form an electron and $HO_2\cdot$, the $HO_2\cdot$ then was dehydrogenized to form $O_2\cdot^-$ (Eqs. (3)–(5)) [36]. However, this self-decomposition process is sluggish and accompanied by a side reaction (Eq. (6)), which is unfavorable to the degradation efficiency. When the $NiFe_2O_4$ NPs decorated on the surface of Ag_3PO_4, the photogenerated H_2O_2 will be catalytically decomposed by the $NiFe_2O_4$ to generate a large amount of $O_2\cdot^-$ and $\cdot OH$ via a photo-Fenton process (Eqs. (8)–(12)) due to the H_2O_2 active properties of $NiFe_2O_4$ under visible light irradiation [39,60]. Accordingly, the signal intensities of $DMPO-O_2\cdot^-$ and $DMPO-\cdot OH$ were enhanced on the 3% $Ag_3PO_4@NiFe_2O_4$ composite. To evidence the decomposition of H_2O_2 by the $NiFe_2O_4$, the compared H_2O_2 yields of pure Ag_3PO_4 and 3% $Ag_3PO_4@NiFe_2O_4$ composite were carried out as following. The sample powder (20 mg) was added into 60 mL 75% CH_3OH solution. The

suspensions were sonicated for 5 min to disperse the photocatalysts completely, followed by stirring under dark for 30 min with air bubbling to achieve the saturated O_2 adsorption. After that, the suspensions were irradiated under visible-light irradiation ($\lambda > 420$ nm). The filtrate of suspension was used to measure the amount of generated H_2O_2 via DPD method. As shown in Fig. 10C, it is clearly that the H_2O_2 yield over the 3% Ag_3PO_4@$NiFe_2O_4$ composite is quite below the Ag_3PO_4, indicating that the H_2O_2 generated on the surface of Ag_3PO_4 were quickly decomposed by the $NiFe_2O_4$. Beyond that, since the recent reports have shown that the steady chemisorption of reactant over catalyst is beneficial for carrier transfer and thus prompt the reactions to occur [61]. We also investigated the surface group variations of 3% Ag_3PO_4@$NiFe_2O_4$ composite via FTIR spectroscopy. As shown in Fig. 10D, the spectra of these Ag_3PO_4@$NiFe_2O_4$ composites present all the peaks of pure Ag_3PO_4 without any big changes and shifts, except a weak peak at about 603 cm^{-1} was observed. By comparing with the spectrum of pure $NiFe_2O_4$, it is believed that this weak peak belongs to the stretching vibration mode of Fe − O [62]. The FTIR spectroscopy results indicated that the surface group variations were not the main reason for the $O_2\cdot^-$ and ·OH generation. According to all above-mentioned results and discussions, we can conclude that besides the direct ·OH formation of hydroxyl oxidized by photoexcited hole on the VB edges of Ag_3PO_4, the Ag_3PO_4@$NiFe_2O_4$ composites open the route of $NiFe_2O_4$-induced H_2O_2 converting into $O_2\cdot^-$ and ·OH over a solid-liquid interfacial photo-Fenton-like reaction, thus the $O_2\cdot^-$ and ·OH

radicals' generation on the Ag_3PO_4@$NiFe_2O_4$ composites systems were greatly enhanced [63].

In order to confirm this in situ solid-liquid interfacial photo-Fenton-like reaction, we further studied the active species of 3% Ag_3PO_4@$NiFe_2O_4$ composite for MO photodegradation via the trapping experiments. In this study, 0.4 mg/mL catalase, 0.01 mM p-benzoquinone (p-BQ), 1 mM isopropanol (IPA) and 1 mM triethanolamine (TEOA) were used as the H_2O_2, $O_2\cdot^-$, ·OH and h$^+$ quenchers, respectively. [53,64]. Furthermore, Ar atmosphere were conducted to reveal the role of ROSs [41]. The results are shown in Fig. 10F, as can be seen, the degradation efficiency was enhanced instead of inhibited when the catalase was added into the system, which can be reasonably explained that the catalase can decompose the photogenerated H_2O_2 and the process of the consumption of photogenerated h$^+_{(Ag_3PO_4)}$ by the adsorbed H_2O_2 on Ag_3PO_4 (Eq. (6)) was decreased, thus promote the accumulation of h$^+_{(Ag_3PO_4)}$ as well as photoactivity. This result also lends support to that the adsorbed H_2O_2 can consume the h$^+_{(Ag_3PO_4)}$ illustrated above. When the IPA was introduced, the degradation efficiency was reduced, indicating the ·OH played an important role in the photocatalysis process. While the degradation efficiency was decreased a lot after the p-BQ was added, suggesting that the $O_2\cdot^-$ played a crucial role in the decomposition of MO under visible light irradiation. When Ar was bubbled into the system, the degradation efficiency was further decreased, which was well consist with the above analysis. Because ·OH and $O_2\cdot^-$ were originated from the O_2 reduction on the CB edges of
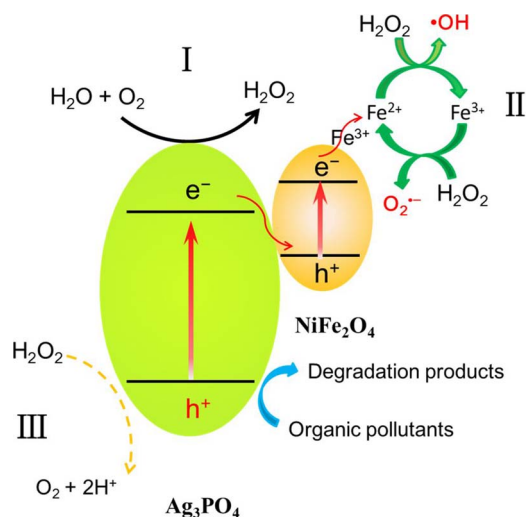
Fig. 11. Proposed mechanism of O-related radicals generation in photocatalytic systems.

Ag_3PO_4, the Ar atmosphere will terminal the O_2 reduction thus decrease the degradation efficiency. In other words, the consumption of $e^-_{(Ag_3PO_4)}$ was been inhibited and the recombination of $e^-_{(Ag_3PO_4)}/h^+_{(Ag_3PO_4)}$ was occurred more easily, therefore, the photocatalytic reaction would be suppressed. In addition, once O_2 is consumed for H_2O_2 production, it would be immediately supplied from air. Accordingly, the rate equation for MO degradation on $Ag_3PO_4@NiFe_2O_4$ composites is first-order. When the TEOA was incorporated into the system, the degradation efficiency was greatly suppressed, unquestionable that $h^+_{(Ag_3PO_4)}$ was the dominant active species in MO degradation process. The trapping examples results indicated that ROSs was an indispensable factor in enhancing the degradation efficiency and the photogenerated $h^+_{(Ag_3PO_4)}$ dominated the degradation efficiencies. At the meantime, it also revealed the eliminating/active decomposition of H_2O_2 on the semiconductors is an important way to promote the photocatalytic activities.

Upon elucidating the reaction process, we conclude the mechanistic pathway as illustrated in Fig. 11. Both Ag_3PO_4 and $NiFe_2O_4$ of the $Ag_3PO_4@NiFe_2O_4$ composites were photo-excited and produced e^-/h^+ pairs under visible-light illumination. After the photo-generated $e^-_{(Ag_3PO_4)}$ of Ag_3PO_4 diffusing to the surface, the $e^-_{(Ag_3PO_4)}$ will react with the adsorbed O_2 and then undergo the protonation process to produce H_2O_2 (I) [65]. If $NiFe_2O_4$ wasn't introduced to this system, these produced H_2O_2 would not be used effectively. It may be diffused into the aqueous solution, but the H_2O_2 was inactive for the organic degradations (Fig. S1). Part of these H_2O_2 could self-decomposition to finally form $O_2\cdot^-$, but this self-decomposition process was sluggish and accompanied by a side reaction (Eq. (6)). Furthermore, the low concentration of H_2O_2 could inhibit the degradation rate of organic pollutants due to the consumption of photogenerated $h^+_{(Ag_3PO_4)}$ by the adsorbed H_2O_2 on Ag_3PO_4 (Eq. (7)) (III), which has been confirmed by the trapping experiments. Therefore, the pure Ag_3PO_4 exhibited a slack photocatalytic activity (Fig. 6). When the $NiFe_2O_4$ NPs were decorated on the surface of Ag_3PO_4, on the one hand, the $NiFe_2O_4$ could specific catalytic decompose H_2O_2 into $O_2\cdot^-$ and $\cdot OH$ species for organic degradation via a photo-Fenton process (Eq. (8)–(12)) (II). More importantly, this decomposition of H_2O_2 decreased the consume of $h^+_{(Ag_3PO_4)}$ by the adsorbed H_2O_2, as a result, more accumulated $h^+_{(Ag_3PO_4)}$ would be used for the pollutants oxidation and bacteria killing, thus superior photocatalytic performance can be gained. On the other hand, the $h^+_{(NiFe_2O_4)}$ can partly eliminate the $e^-_{(Ag_3PO_4)}$ on the surface of Ag_3PO_4 and improve the stability (Fig. S7).

4. Conclusions

In summary, we report a simple and green strategy for evenly decorating $NiFe_2O_4$ NPs on the surface of Ag_3PO_4 particles. The $NiFe_2O_4$ NPs possess specific in catalyzing decomposition of H_2O_2 via a photo-Fenton process, which can effectively catalyze the H_2O_2 that generated on the surface of Ag_3PO_4 into $O_2\cdot^-$ and $\cdot OH$ radicals. The timely decomposition of H_2O_2 not only produced strong oxidative capacity $O_2\cdot^-$ and $\cdot OH$ radicals which could play a major role in the organic photodegradation process but also reduced the consumption of $h^+_{(Ag_3PO_4)}$ by the adsorbed H_2O_2. As a result, this approach has efficiently enhanced the photocatalytic performance. This work thus clearly demonstrates that the surface catalysis engineering can serve as a versatile approach to refine catalysts, in efforts to promote the production of $O_2\cdot^-$ and $\cdot OH$ radicals and develop high efficient photocatalysts. In addition, because the $h^+_{(NiFe_2O_4)}$ can partly quench the electrons on the surface of Ag_3PO_4, the reduction of Ag^+ ions in Ag_3PO_4 to Ag metal could be slowed down and improved the stability of Ag_3PO_4. More importantly, the $NiFe_2O_4$ itself possesses magnetic properties, so the $Ag_3PO_4@NiFe_2O_4$ composite can be separated from solutions easily via a magnetic field. The concept demonstrated here mainly highlights the importance of catalytic reaction step on semiconductor surface in the whole photocatalysis process, of which the eliminating/active decomposition of H_2O_2 on the semiconductors is an important way to promote the photocatalytic activities.

Appendix A. Supplementary data

Supplementary data associated with this article can be found, in the online version, at http://dx.doi.org/10.1016/j.apcatb.2017.11.045.

References

[1] J. Schneider, M. Matsuoka, M. Takeuchi, J. Zhang, Y. Horiuchi, M. Anpo, D.W. Bahnemann, Chem. Rev. 114 (2014) 9919–9986.
[2] S. Chu, Y. Cui, N. Liu, Nat. Mater. 16 (2016) 16–22.
[3] D. Wang, D. Astruc, Chem. Rev. 114 (2014) 6949–6985.
[4] F. Dong, Z. Wang, Y. Li, W.-K. Ho, S.C. Lee, Environ. Sci. Technol. 48 (2014) 10345–10353.
[5] S. Bai, J. Jiang, Q. Zhang, Y. Xiong, Chem. Soc. Rev. 44 (2015) 2893–2939.
[6] F. Dong, T. Xiong, Y. Sun, L. Lu, Y. Zhang, H. Zhang, H. Huang, Y. Zhou, Z. Wu, Appl. Catal. B: Environ. 219 (2017) 450–458.
[7] S.T. Kochuveedu, Y.H. Jang, D.H. Kim, Chem. Soc. Rev. 42 (2013) 8467–8493.
[8] S. Kundu, A. Patra, Chem. Rev. 117 (2017) 712–757.
[9] R. Asahi, T. Morikawa, T. Ohwaki, K. Aoki, Y. Taga, Science 293 (2001) 269–271.
[10] F. Dong, Z. Zhao, Y. Sun, Y. Zhang, S. Yan, Z. Wu, Environ. Sci. Technol. 49 (2015) 12432–12440.
[11] L. Wang, S. Liu, Z. Wang, Y. Zhou, Y. Qin, Z.L. Wang, ACS Nano 10 (2016) 2636–2643.
[12] H. Huang, B. Dai, W. Wang, C. Lu, J. Kou, Y. Ni, L. Wang, Z. Xu, Nano Lett. 17 (2017) 3803–3808.
[13] H. Li, Y. Sang, S. Chang, X. Huang, Y. Zhang, R. Yang, H. Jiang, H. Liu, Z.L. Wang, Nano Lett. 15 (2015) 2372–2379.
[14] C. Tan, X. Cao, X.J. Wu, Q. He, J. Yang, X. Zhang, J. Chen, W. Zhao, S. Han, G.H. Nam, M. Sindoro, H. Zhang, Chem. Rev. 117 (2017) 6225–6331.
[15] X. She, J. Wu, J. Zhong, H. Xu, Y. Yang, R. Vajtai, J. Lou, Y. Liu, D. Du, H. Li, P.M. Ajayan, Nano Energy 27 (2016) 138–146.
[16] M. Rahman, K. Davey, S.Z. Qiao, Small 13 (2017) 1700376.
[17] J. Li, G. Zhan, Y. Yu, L. Zhang, Nat. Commun. 7 (2016) 11480.
[18] D. Deng, K.S. Novoselov, Q. Fu, N. Zheng, Z. Tian, X. Bao, Nat. Nanotechnol. 11 (2016) 218–230.
[19] D. Yang, J. Feng, L. Jiang, X. Wu, L. Sheng, Y. Jiang, T. Wei, Z. Fan, Adv. Funct. Mater. 25 (2015) 7080–7087.
[20] L. Lin, H. Ou, Y. Zhang, X. Wang, ACS Catal. 6 (2016) 3921–3931.

[21] K. Schwinghammer, M.B. Mesch, V. Duppel, C. Ziegler, J. Senker, B.V. Lotsch, J. Am. Chem. Soc. 136 (2014) 1730–1733.

[22] H. Ou, L. Lin, Y. Zheng, P. Yang, Y. Fang, X. Wang, Adv. Mater. 29 (2017) 1700008.

[23] W.J. Ong, L.L. Tan, Y.H. Ng, S.T. Yong, S.P. Chai, Chem. Rev. 116 (2016) 7159–7329.

[24] S. Gligorovski, R. Strekowski, S. Barbati, D. Vione, Chem. Rev. 115 (2015) 13051–13092.

[25] M. Hayyan, M.A. Hashim, I.M. AlNashef, Chem. Rev. 116 (2016) 3029–3085.

[26] G. Jiang, X. Li, M. Lan, T. Shen, X. Lv, F. Dong, S. Zhang, Appl. Catal. B: Environ. 205 (2017) 532–540.

[27] C. Liu, D. Kong, P.C. Hsu, H. Yuan, H.W. Lee, Y. Liu, H. Wang, S. Wang, K. Yan, D. Lin, P.A. Maraccini, K.M. Parker, A.B. Boehm, Y. Cui, Nat. Nanotechnol. 11 (2016) 1098–1104.

[28] Z. Yi, J. Ye, N. Kikugawa, T. Kako, S. Ouyang, H. Stuart-Williams, H. Yang, J. Cao, W. Luo, Z. Li, Y. Liu, R.L. Withers, Nat. Mater. 9 (2010) 559–564.

[29] X. Ma, B. Lu, D. Li, R. Shi, C. Pan, Y. Zhu, J. Phys. Chem. C 115 (2011) 4680–4687.

[30] Y. Bi, S. Ouyang, N. Umezawa, J. Cao, J. Ye, J. Am. Chem. Soc. 133 (2011) 6490–6492.

[31] D.J. Martin, G. Liu, S.J. Moniz, Y. Bi, A.M. Beale, J. Ye, J. Tang, Chem. Soc. Rev. 44 (2015) 7808–7828.

[32] G.-y. Zhao, L.-j. Liu, J.-r. Li, Q. Liu, J. Alloys Compd. 664 (2016) 169–174.

[33] Santosh S. Patil, Mohaseen S. Tamboli, Virendrakumar G. Deonikar, Govind G. Umarji, Jalindar D. Ambekar, Milind V. Kulkarni, Sanjay S. Kolekar, Bharat B. Kale, D.R. Patil, Dalton Trans. 44 (2015) 20426–20434.

[34] J. Sheng, X. Li, Y. Xu, ACS Catal. 4 (2014) 732–737.

[35] H. Katsumata, M. Taniguchi, S. Kaneco, T. Suzuki, Catal. Commun. 34 (2013) 30–34.

[36] Y. Zhang, C. Liu, B. Xu, F. Qi, W. Chu, Appl. Catal. B: Environ. 199 (2016) 447–457.

[37] Y. Liu, Y. Zhu, J. Xu, X. Bai, R. Zong, Y. Zhu, Appl. Catal. B: Environ. 142–143 (2013) 561–567.

[38] P. Annie Vinosha, B. Xavier, A. Ashwini, L. Ansel Mely, S. Jerome Das, Optik 137 (2017) 244–253.

[39] H. Ji, X. Jing, Y. Xu, J. Yan, H. Li, Y. Li, L. Huang, Q. Zhang, H. Xu, H. Li, RSC Adv. 5 (2015) 64299.

[40] Y. Ahmed, Z. Yaakob, P. Akhtar, Catal. Sci. Technol. 6 (2016) 1222–1232.

[41] Y. Li, S. Ouyang, H. Xu, X. Wang, Y. Bi, Y. Zhang, J. Ye, J. Am. Chem. Soc. 138 (2016) 13289–13297.

[42] S. Huang, Y. Xu, Q. Liu, T. Zhou, Y. Zhao, L. Jing, H. Xu, H. Li, Appl. Catal. B: Environ. 218 (2017) 174–185.

[43] S. Huang, Y. Xu, Z. Chen, M. Xie, H. Xu, M. He, H. Li, Q. Zhang, RSC Adv. 5 (2015) 71035–71045.

[44] M.-Y. Ye, Z.-H. Zhao, Z.-F. Hu, L.-Q. Liu, H.-M. Ji, Z.-R. Shen, T.-Y. Ma, Angew. Chem. Int. Ed. 56 (2017) 1–6.

[45] Y. Xu, T. Zhou, S. Huang, M. Xie, H. Li, H. Xu, J. Xia, H. Li, RSC Adv. 5 (2015) 41475–41483.

[46] S. Huang, Y. Xu, M. Xie, Q. Liu, H. Xu, Y. Zhao, M. He, H. Li, RSC Adv. 7 (2017) 30845–30854.

[47] Y. Zhao, B. Zhao, J. Liu, G. Chen, R. Gao, S. Yao, M. Li, Q. Zhang, L. Gu, J. Xie, X. Wen, L.-Z. Wu, C.-H. Tung, D. Ma, T. Zhang, Angew. Chem. Int. Ed. 55 (2016) 4215–4219.

[48] J. Wang, G. Yang, L. Wang, W. Yan, J. Mater. Chem. A 4 (2016) 8620–8629.

[49] B.S. Holinsworth, D. Mazumdar, H. Sims, Q.C. Sun, M.K. Yurtisigi, S.K. Sarker, A. Gupta, W.H. Butler, J.L. Musfeldt, Appl. Phys. Lett. 103 (2013) 082406.

[50] L. Jing, Y. Xu, S. Huang, M. Xie, M. He, H. Xu, H. Li, Q. Zhang, Appl. Catal. B: Environ. 199 (2016) 11–22.

[51] T. Yan, J. Tian, W. Guan, Z. Qiao, W. Li, J. You, B. Huang, Appl. Catal. B: Environ. 202 (2017) 84–94.

[52] Z.-M. Yang, G.-F. Huang, W.-Q. Huang, J.-M. Wei, X.-G. Yan, Y.-Y. Liu, C. Jiao, Z. Wan, A. Pan, J. Mater. Chem. A 2 (2014) 1750–1756.

[53] C. Tang, E. Liu, J. Wan, X. Hu, J. Fan, Appl. Catal. B: Environ. 181 (2016) 707–715.

[54] Y. He, L. Zhang, B. Teng, M. Fan, Environ. Sci. Technol. 49 (2015) 649–656.

[55] L. Liu, L. Ding, Y. Liu, W. An, S. Lin, Y. Liang, W. Cui, Appl. Catal. B: Environ. 201 (2017) 92–104.

[56] A. Ren, C. Liu, Y. Hong, W. Shi, S. Lin, P. Li, J. Chem. Eng. 258 (2014) 301–308.

[57] K. Iwashina, A. Iwase, Y.H. Ng, R. Amal, A. Kudo, J. Am. Chem. Soc. 137 (2015) 604–607.

[58] B. Wang, J. Di, P. Zhang, J. Xia, S. Dai, H. Li, Appl. Catal. B: Environ. 206 (2017) 127–135.

[59] Y. Kofuji, Y. Isobe, Y. Shiraishi, H. Sakamoto, S. Tanaka, S. Ichikawa, T. Hirai, J. Am. Chem. Soc. 138 (2016) 10019–10025.

[60] Y. Deng, M. Xing, J. Zhang, Appl. Catal. B: Environ. 211 (2017) 157–166.

[61] N. Zhang, X. Li, H. Ye, S. Chen, H. Ju, D. Liu, Y. Lin, W. Ye, C. Wang, Q. Xu, J. Zhu, L. Song, J. Jiang, Y. Xiong, J. Am. Chem. Soc. 138 (2016) 8928–8935.

[62] S. Huang, Y. Xu, M. Xie, H. Xu, M. He, J. Xia, L. Huang, H. Li, Colloids Surf. A: Physicochem. Eng. Asp. 478 (2015) 71–80.

[63] B. Qiu, M. Xing, J. Zhang, J. Mater. Chem. A 3 (2015) 12820–12827.

[64] D. Xia, T. An, G. Li, W. Wang, H. Zhao, P.K. Wong, Water Res. 99 (2016) 149–161.

[65] H. Sheng, H. Zhang, W. Song, H. Ji, W. Ma, C. Chen, J. Zhao, Angew. Chem. Int. Ed. 54 (2015) 5905–5909.